RESEARCH ARTICLE
ATMOSPHERIC PHYSICS

Earth and Planetary Physics
10: 472–481, 2026
doi: 10.26464/epp2026039

An efficient model to estimate thermospheric mass density based on an artificial intelligence approach

DongFang Zhai[1], Wei Xu[1*], HaiBing Ruan[2*], XuDong Gu[1], BinBin Ni[1], ShiWei Wang[1], JingYuan Feng[1], Wen Cheng[1], YuDi Pan[1], WenChen Ma[1], HaoTian Xu[1], and HanQing Shi[1]

[1]School of Earth and Space Science and Technology, Wuhan University, Wuhan 430072, China;

[2]Institute of Space Weather, Nanjing University of Information Science and Technology, Nanjing 210044, China

Key Points:

- A thermospheric mass density estimation model is developed using a modified U-Net architecture.
- The model provides data-driven global thermospheric density estimations across altitudes from 100 to 500 km.
- The model serves as a computationally efficient alternative to the Thermosphere–Ionosphere–Electrodynamics General Circulation Model (TIEGCM) for thermospheric density simulations, offering significant speedup with comparable accuracy.

Citation: Zhai, D. F., Xu, W., Ruan, H. B., Gu, X. D., Ni, B. B., Wang, S. W., Feng, J. Y., Cheng, W., Pan, Y. D., … Shi, H. Q. (2026). An efficient model to estimate thermospheric mass density based on an artificial intelligence approach. *Earth Planet. Phys.*, *10*(3), 472–481. http://doi.org/10.26464/epp2026039

Abstract: Modeling the mass density of the thermosphere is essential for understanding the upper atmospheric dynamics and for supporting satellites and the space station. Such modeling has traditionally relied on either empirical approaches or first-principles physics-based frameworks. The empirical models are computationally efficient with relatively lower accuracy, whereas the physics-based models are more accurate with the cost of computation time. In this study, a data-driven deep learning model based on a modified U-Net architecture is proposed to estimate the global thermospheric mass density at altitudes of 100 to 500 km. This model directly utilizes input features including time, spatial coordinates, geomagnetic indices, the $F_{10.7}$ solar flux, and the solar wind speed. To improve the model performance, we have introduced three main components: a gated recurrent unit-enhanced attention mechanism for spatially adaptive feature refinement, a height-adaptive normalization technique to mitigate altitude-induced bias, and a hybrid loss function combining mean absolute error with Laplacian loss to preserve both the global structure and fine-scale details. The proposed model achieves accuracy comparable to physics-based models such as the Thermosphere–Ionosphere–Electrodynamics General Circulation Model (TIEGCM), with percentage errors typically below 5%, while the simulation time has been dramatically reduced from tens of minutes to a few seconds. This framework provides an efficient and accurate tool for reconstructing the global thermospheric density and can potentially be utilized for real-time estimation of the thermosphere density under varying geomagnetic and solar conditions.

Keywords: thermosphere; deep learning; U-Net

1. Introduction

The thermosphere, which extends from the mesopause to approximately 1000 km altitude, represents a critical region of Earth's upper atmosphere (Powell, 2018). In this rarefied layer, molecular diffusion governs the vertical distribution of atmospheric constituents, leading to a nonuniform composition in which both mean molecular weight and mass density decrease exponentially with altitude (Lei JH et al., 2023). Solar extreme ultraviolet and far ultraviolet radiation serve as the primary energy sources driving thermal expansion and variability in thermospheric density (Richards et al., 1981; Prölss, 2011). In addition to solar forcing, geomagnetic activity strongly modulates thermospheric conditions, typically leading to density enhancements during periods of elevated geomagnetic disturbance (Jacchia, 1959; Liu X et al., 2014). These responses are primarily caused by the dissipation of magnetospheric electric fields and enhanced precipitation of energetic particles into the upper atmosphere (Prölss, 1997; Wang X et al., 2020). Upward-propagating atmospheric waves from the lower atmosphere also play an important role in shaping thermospheric dynamics (Hedin, 1979).

Despite the low density of the thermosphere, it exerts significant aerodynamic drag on spacecraft in low Earth orbit, making accurate thermospheric density modeling essential for satellite orbit prediction and maneuver planning. Various techniques have been developed to estimate thermospheric mass density. The most established method involves analyzing drag-induced orbital perturbations, which enable indirect retrieval of density. Widely

---

First author: D. F. Zhai, dongfangz@whu.edu.cn
Correspondence to: W. Xu, wei.xu@whu.edu.cn
H. B. Ruan, rhb@nuist.edu.cn
Received 11 NOV 2025; Accepted 11 FEB 2025.

used approaches include orbit-derived density estimation (McLaughlin et al., 2011), accelerometer-based techniques (Bruinsma et al., 2014), and ballistic coefficient inversion (Mehta et al., 2014). In addition, complementary observations from instruments such as neutral mass spectrometers, ultraviolet imagers, and incoherent scatter radars provide valuable pointwise measurements (Emmert, 2015). However, these measurements are often limited in spatial and temporal coverage, making them insufficient for reconstructing global, time-resolved thermospheric density fields.

To overcome these limitations, both empirical and physics-based models have been developed. These models integrate various data sources, including satellite-based mass spectrometers, incoherent scatter radar-derived temperatures, solar occultation profiles, and solar activity indices. Among the empirical models, the Mass Spectrometer and Incoherent Scatter (MSIS) series, originally proposed by Hedin et al. (1977) and later refined (Hedin, 1983, 1987; Picone et al., 2002), remains the most widely used. It provides estimates of total mass density, neutral temperature, and major species such as atomic oxygen and molecular nitrogen (Emmert et al., 2022). Similarly, the Drag Temperature Model family (Barlier et al., 1978; Bruinsma, 2015; Bruinsma and Boniface, 2021) has evolved from drag-derived data to incorporate accelerometer measurements and airglow remote sensing. The Jacchia models (Jacchia, 1965, 1970; Bowman et al., 2008) use satellite drag data to simulate vertical profiles of thermospheric temperature and density, driven primarily by $F_{10.7}$ (solar radio flux at 10.7 cm) and geomagnetic indices such as *Kp* (planetary *K*) and *AE* (auroral electrojet).

In contrast, physics-based models solve first-principles equations of fluid dynamics and thermodynamics to simulate thermospheric conditions. These models require detailed inputs, such as the solar extreme ultraviolet flux, lower boundary forcing, and gravity wave parameters. Representative models include the Global Ionosphere–Thermosphere Model (GITM; Ridley et al., 2006), the Thermosphere–Ionosphere–Electrodynamics General Circulation Model (TIEGCM; Qian LY et al., 2014), and the Whole Atmosphere Community Climate Model with thermosphere and ionosphere extension (WACCM-X; Liu HL et al., 2010), which are capable of propagating space weather disturbances through physically consistent processes. These models outperform empirical approaches under disturbed conditions, where empirical simulations may deviate by more than 40%, although this comes at the cost of significantly increased computational time.

Although empirical models offer fast computation, their accuracy degrades during geomagnetically active periods because of inherent nonlinearities and limited adaptability. Physics-based models are more reliable under such conditions but are computationally intensive, making them less suitable for operational or real-time applications. Recent advances in artificial intelligence have introduced data-driven modeling approaches as promising alternatives for complex geophysical systems. These models can achieve accuracy comparable to first-principles simulations while substantially reducing computational time (Shi HQ et al., 2025). For example, the NRLMSIS 2.0 (U.S. Naval Research Laboratory Mass Spectrometer and Incoherent Scatter radar version 2.0) model incorporates machine learning calibration to reduce density prediction bias by up to 25% during geomagnetic storms (Licata et al., 2022; Li YP et al., 2024). Recurrent neural networks have been utilized to forecast storm-time ionospheric irregularities (Xiong P et al., 2021), whereas generative models have been used to reconstruct incomplete total electron content maps with improved spatial continuity (Chen Z et al., 2019). Intelligent particle filtering algorithms have also been developed to calibrate uncertain parameters in physics-based models, enhancing forecast reliability (Ren DX and Lei JH, 2022). Additionally, ensemble learning models such as MBiLE (Multilayer Perceptron and bi-directional Long Short-Term Memory for ensemble learning), which combine Bi-LSTM (Bidirectional Long Short-Term Memory) and MLP (Multilayer Perceptron) architectures, have demonstrated strong predictive capabilities for thermospheric mass density (Pan Q et al., 2024). Another notable example is the use of artificial neural networks that significantly outperform empirical models in capturing thermospheric variability (Weng LB et al., 2020).

These studies collectively demonstrate the potential of machine learning models to complement or, in certain cases, replace traditional modeling frameworks. Motivated by these advancements, here we aim to develop a data-driven deep learning model for global thermospheric mass density estimation. The proposed approach seeks to achieve accuracy comparable to that of the TIEGCM model while substantially reducing computational time, offering a practical and efficient solution for operational space weather applications across diverse geophysical conditions.

2. Dataset and Procedures

In this study, thermospheric mass density data were obtained from the TIEGCM. Operating over an altitude range of 90–700 km, the TIEGCM provides high-resolution, three-dimensional outputs of neutral mass density, horizontal wind fields, temperature profiles, ion drag, and conductivity parameters. The model is driven primarily by inputs such as the $F_{10.7}$ solar flux, *Kp* index, *Ap* (planetary *A*) index, and lower boundary conditions. Crucially, the TIEGCM incorporates dynamic coupling with ionospheric electrodynamics, enabling physically realistic simulations of thermospheric responses to geomagnetic storms, substorms, and solar cycle variability (Ruan HB et al., 2018; Li Z et al., 2019). The model supports both serial and parallel computing modes on Linux-based workstations. Using 16 CPU (central processing unit) cores, the simulation of one day of thermospheric density typically requires approximately 3 hours. The global thermospheric mass density outputs from the TIEGCM are used as training data for the proposed deep learning model.

A series of TIEGCM simulations were conducted to identify the most relevant auxiliary variables for thermospheric mass density prediction. By systematically varying candidate input parameters and applying a controlled-variable approach, the sensitivity of the thermospheric density to different drivers was assessed. This analysis revealed that altitude, geographic latitude and longitude, local solar time, the $F_{10.7}$ index, and the *Kp* index were the dominant influencing factors. These findings align with established physical understanding and prior studies, and these variables were selected as the core inputs for the machine learning framework.

To generate sufficient training data, TIEGCM simulations were performed for the full year of 2013 at a spatial resolution of 5° × 5° (longitude × latitude). The model was driven by daily $F_{10.7}$ values, 3-hourly Kp indices, and the empirical high-latitude electric field model of Heelis et al. (1982). Full-year coverage ensures comprehensive representation of seasonal variability in thermospheric density. The output data were stored in NetCDF (Network Common Data Form) as four-dimensional arrays (longitude × latitude × pressure altitude × universal time). After processing, the thermospheric mass density fields were gridded at 72 × 36 (longitude × latitude) with an hourly temporal resolution and covered the altitude range from 100 to 500 km.

Additional space weather parameters used as inputs for the deep learning model were obtained from the OMNI database. The final set of input features included day of the year, universal time, geographic coordinates, the daily $F_{10.7}$ index ($F_{10.7\mathrm{d}}$), the 81-day centered average $F_{10.7}$ ($F_{10.7\mathrm{a}}$), the Kp index, the solar wind speed, and the interplanetary magnetic field B_z component (Santoso et al., 2025). The target output was thermospheric mass density. The dataset comprised 876,000 samples. These were partitioned on a monthly basis into training, validation, and test sets using a 7:1.5:1.5 ratio. To enhance temporal independence, samples in the training and validation sets were grouped into daily blocks and randomly shuffled prior to model training.

3. Model Construction

Deep learning utilizes artificial neural networks with multiple hierarchical layers to simulate the brain's process of extracting increasingly abstract features through nonlinear transformations (Walczak, 2019). Unlike traditional machine learning, which relies heavily on manual feature engineering (Wang P et al., 2021), deep learning models autonomously learn features from unstructured data (LeCun et al., 2015). They are particularly effective in leveraging large-scale unlabeled datasets through unsupervised or self-supervised learning, albeit at the cost of higher computational demands. Enabled by advances in artificial intelligence, deep learning has achieved remarkable success in domains such as image recognition (Krizhevsky et al., 2017), speech recognition (Hinton et al., 2012), and natural language processing (Sutskever et al., 2014). In the field of space physics, these techniques have been applied to problems such as thermospheric density prediction, total electron content estimation (Ren XC et al., 2024), and sporadic E layer detection (Yu BK et al., 2025). Among the representative architectures, convolutional neural networks (CNNs; LeCun et al., 1998), recurrent neural networks (Lipton et al., 2015), and generative adversarial networks (Goodfellow et al., 2020) are widely used. Convolutional neural networks, in particular, excel through local connectivity and weight sharing, which significantly reduce model complexity, improve generalization, and simplify optimization.

Building on these advantages, here we adopt the U-Net architecture, a CNN-based model originally developed for biomedical image segmentation (Ronneberger et al., 2015; Azad et al., 2024). The U-Net architecture addresses challenges posed by limited labeled data through its encoder–decoder structure and compatibility with data augmentation techniques (Trebeschi et al., 2017; Xie B et al., 2024). The architecture features a symmetric design: a contracting path (encoder) for extracting semantic features via convolution and downsampling, and an expanding path (decoder) for spatial reconstruction through upsampling and convolution. Crucially, skip connections link corresponding levels of the encoder and decoder, enabling multi-scale feature fusion and enhancing pixel-level prediction accuracy. This integration of deep contextual understanding with fine spatial detail makes U-Net particularly suitable for tasks requiring precise spatial resolution, such as those in geophysical and space environment modeling.

The U-Net-inspired architecture used in this study is schematically illustrated in Figure 1. It processes 10 input tensors, each with a spatial resolution of 36 × 72 pixels. Both the encoder and decoder paths utilize sequential 3 × 3 convolutional modules (light blue arrows in Figure 1) to extract localized features and reconstruct hierarchical representations. Each convolution is followed by a batch normalization layer (black squares), which stabilizes feature distributions and mitigates vanishing gradients (Ioffe and Szegedy, 2015). In the encoder (left branch), 2 × 2 max-pooling layers (yellow downward arrows) downsample the feature maps, reducing spatial resolution while doubling channel depth. The decoder (right branch) applies 2 × 2 transposed convolutions (yellow upward arrows) to upsample the feature maps, restoring spatial resolution and reducing channel depth for precise reconstruction.

A key modification to the standard U-Net is the inclusion of a gated attention mechanism at the bottleneck (orange arrows in Figure 1). This mechanism dynamically computes spatial attention weights through interactions between encoder features and a learned gating signal. The resulting attention map emphasizes task-relevant features while suppressing noise, enhancing contextual awareness during decoding. The final layer is a 1 × 1 convolution (dark blue arrow) that maps the high-dimensional output to a single-channel simulation.

The model was implemented in Python 3.9 using PyTorch. Training was conducted for up to 500 epochs to ensure sufficient optimization, with early stopping triggered if validation loss stagnated for 7 consecutive epochs (Prechelt, 2012), helping prevent overfitting and reduce unnecessary computation. The Adam optimizer was used with an initial learning rate of 0.001, providing stable convergence in complex loss landscapes (Kingma and Ba LJ, 2015). Additionally, an adaptive learning rate schedule was applied, halving the rate (factor = 0.5) after 3 stagnant epochs to improve convergence near optima and avoid local minima.

Conventional normalization techniques are applied to thermospheric mass density data to improve the simulated capability at lower heights. Specifically, a height-adaptive normalization method is proposed for the thermospheric density data. This model provides the expected theoretical density value, $\rho(h)$, as a function of altitude. For each observed density value $\rho_{\mathrm{obs}}(h)$ at a specific altitude h, the normalized density is computed by using the following formula:

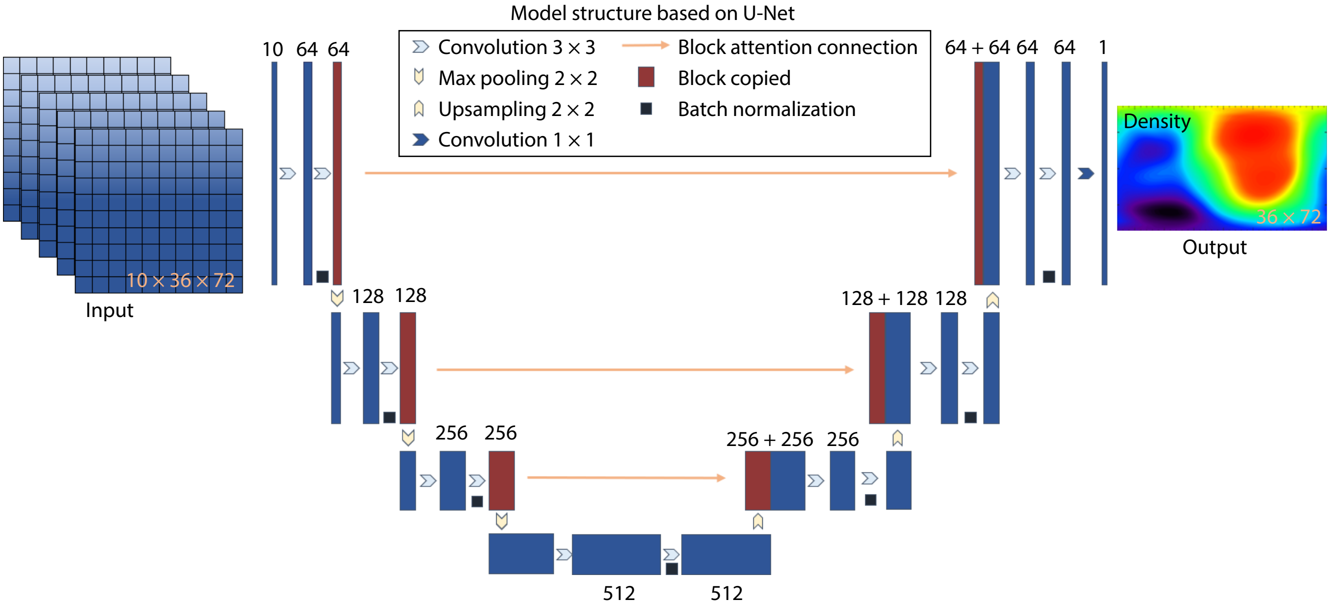

Figure 1. Outline of the model structure based on the U-Net architecture. DOY, day of the year.

$$\text{Target} = \log\left(\rho_{\text{obs}}(h)\right) - \log\left(\rho(h)\right). \tag{1}$$

By computing density residuals relative to the reference model, the dominant exponential altitude dependence is effectively decoupled from the model's learning objective. This approach transforms the simulation task from direct modeling of exponentially varying absolute density to modeling relative deviations from a known altitude-dependent baseline. Consequently, the influence of altitude on observed values is substantially mitigated, thereby enhancing the model's sensitivity to other atmospheric variables across all altitude ranges.

The loss function utilized in the present model training contains two equally weighted components. The first component is the mean absolute error (MAE), defined as the mean of absolute differences between simulated and target values:

$$L_{\text{MAE}} = \frac{1}{N}\sum_{i=1}^{N}\left|Y_i^{\text{obs}} - Y_i^{\text{est}}\right|. \tag{2}$$

where N denotes the total number of samples, i is the sample index, Y_i^{obs} represents the observed or target values of the i-th sample, and Y_i^{est} represents the corresponding estimated values predicted by the model. The second component is the Laplacian loss function, which is a loss function used in image processing tasks (Hou QQ and Liu F, 2019). It maintains scale-invariant sensitivity to global structural discrepancies by constructing Gaussian pyramids and Laplacian pyramids. The Laplacian formula is specifically as follows:

$$L_{\text{lap}} = \sum_{i=1}^{N} 2^{i-1}\left\|L^i(\hat{a}) - L^i(a)\right\|_1. \tag{3}$$

In Equation (3), N denotes the total number of pyramid levels, i is the pyramid level index, $L^i(\hat{a})$ represents the Laplacian pyramid representation at the i-th level, $\hat{a}$ denotes the predicted output, a denotes the target output. The formula for the final loss function is as follows:

$$L = 0.5L_{\text{MAE}} + 0.5L_{\text{lap}}. \tag{4}$$

This loss function integrates the global and local components computed simultaneously, thereby enhancing the model's capacity to preserve both detailed and global information within images. Figure 2 shows the change in loss values for the training and test sets during the iteration process.

4. Model Validation and Evaluation

To evaluate model performance, we compared its outputs with the testing dataset under varying seasonal, geomagnetic, and solar conditions. The analysis focuses on two representative altitudes: 200 km and 500 km. Figure 3a presents the temporal variations of the Kp and $F_{10.7}$ indices throughout 2013. Figures 3b and 3d display the thermospheric density simulated by the TIEGCM at 200 km and 500 km, respectively, whereas Figures 3c and 3e show the corresponding results from our model. As shown in Figures 3b

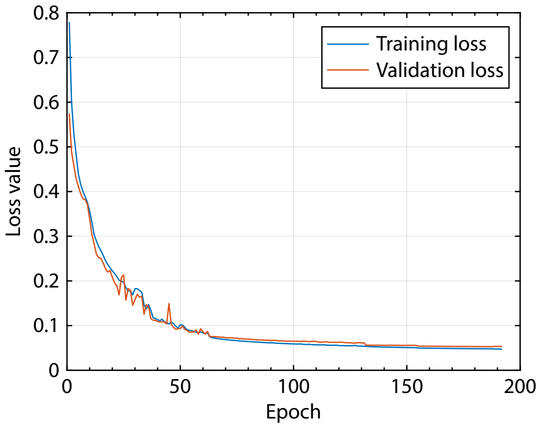

Figure 2. The values of the loss function after the training shown in the legend.

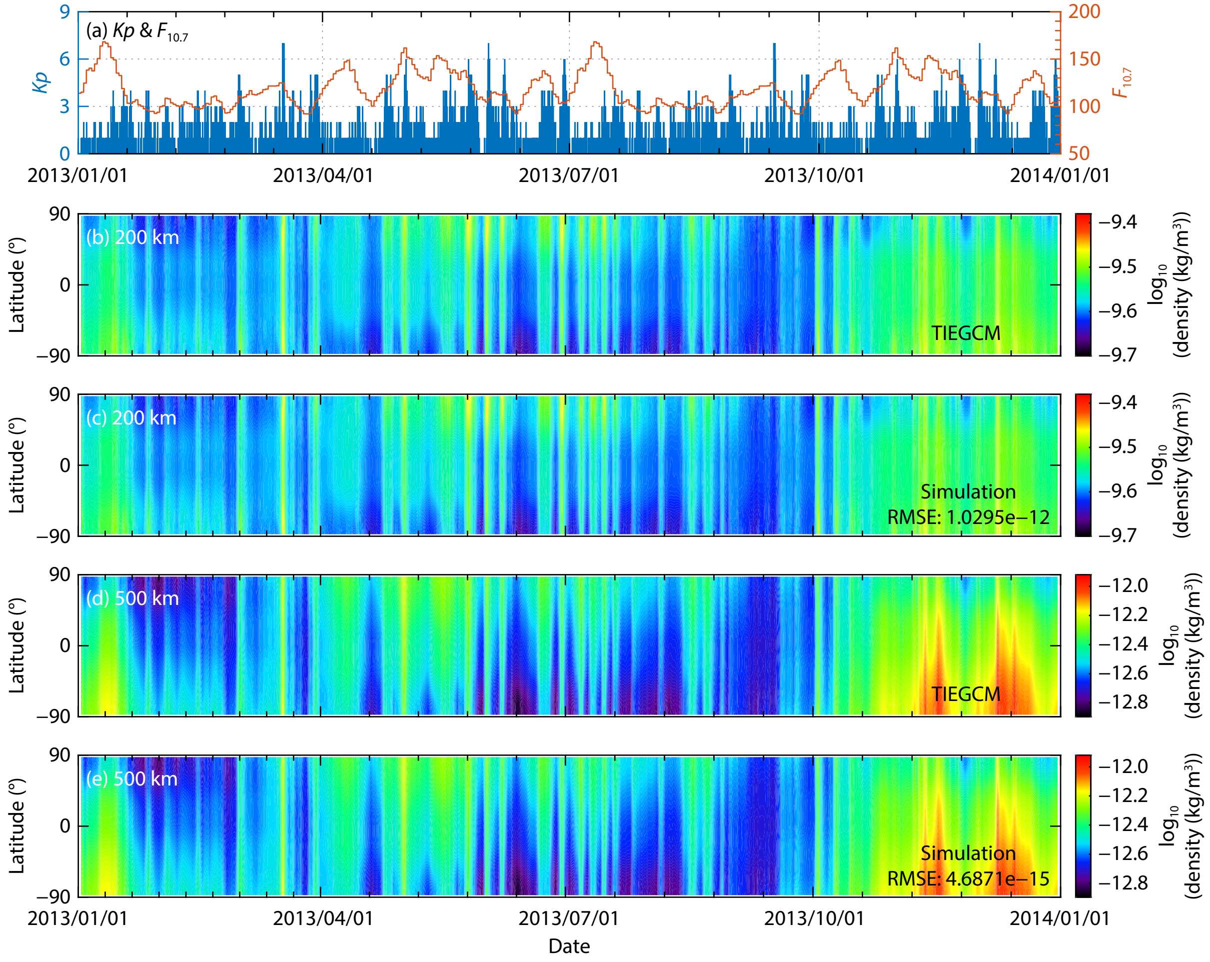

Figure 3. (a) Temporal variations of the *Kp* index and $F_{10.7}$ solar flux during the study period. (b, d) Longitudinally averaged thermospheric mass densities at altitudes of 200 km and 500 km, respectively, derived from the TIEGCM. (c, e) Corresponding thermospheric mass densities at the same altitudes, simulated by the deep learning model. The RMSE values for the model accuracy are indicated in panels (c) and (e).

and 3d, seasonal variability in the thermospheric density becomes more pronounced at higher altitudes, a feature accurately captured by our model. The root mean square error (RMSE) between the TIEGCM and model output is 1.03×10^{-18} at 200 km and as low as 4.69×10^{-18} at 500 km, indicating strong agreement and high fidelity of the proposed model.

Figure 4 illustrates the pronounced seasonal variability of the thermospheric density at an altitude of 300 km during local noon (12:00 LT) across four key seasonal epochs: March equinox, June solstice, September equinox, and December solstice (from top to bottom). Each row presents three panels: the first shows the TIEGCM-simulated density, the second displays results from our model, and the third depicts the difference between the two. All maps represent the logarithmic values of thermospheric density in kilograms per cubic meter. Overall, the density distributions produced by our model closely match those of the TIEGCM. As shown in the first two columns, both enhanced and depleted density regions align well across all seasons. Minor discrepancies are evident in the third column, particularly at high latitudes (>80°), which are likely attributable to moderate geomagnetic storms occurring during these periods.

To further evaluate the robustness of the model, we tested its performance under storm-time conditions. Figure 5 compares the thermospheric density at 100 km, 300 km, and 500 km between the TIEGCM (first row) and our model (second row) during a geomagnetic storm with a *Kp* index of 7. The density distribution exhibits pronounced equatorial symmetry, particularly at higher altitudes (Figures 5e, 5f, 5i, 5j), consistent with previous findings (Li RX and Lei JH, 2021). The third row of Figure 5 shows the point-wise differences between the two models, whereas the fourth row presents the meridionally averaged differences. Quantitatively, the percentage error between the TIEGCM and our model remains low: within ±0.2% at 100 km, ±1% at 300 km, and up to 4.3% at 500 km. These differences are primarily attributed to the data imbalance in the training set, where storm-time samples represent less than 15%, compared with more than 85% from quiet-time conditions. Despite this, the overall percentage error remains below 5%, with a mean error of less than 1.2%, highlighting the model's strong generalization and reliability even during disturbed geomagnetic conditions.

Under geomagnetically quiet conditions (typically defined as $Kp \leq 3$), the model exhibits strong consistency with the TIEGCM results across multiple altitudes. Figure 6 presents a representative case

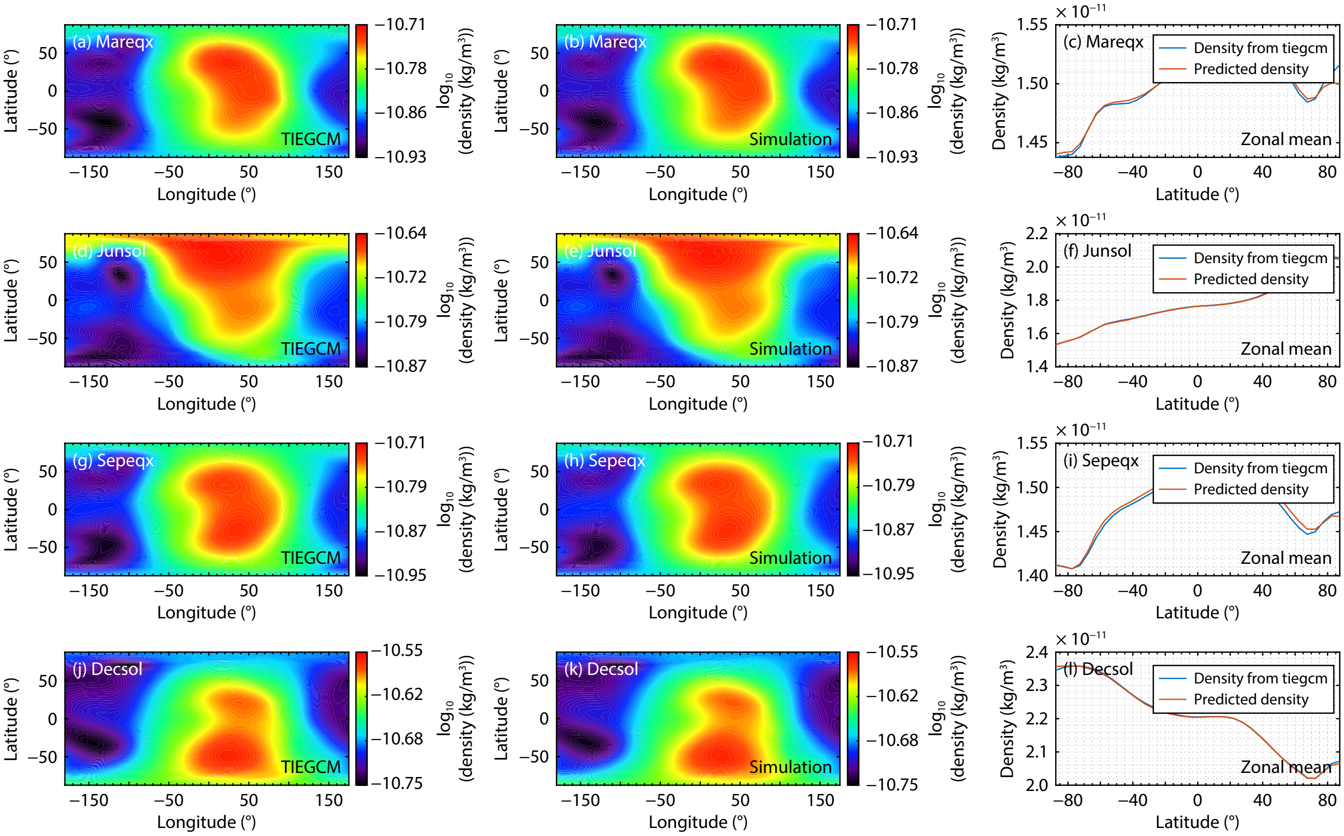

Figure 4. Seasonal sensitivity of the performance of the TIEGCM model and the deep learning model. Four representative seasonal months are selected.

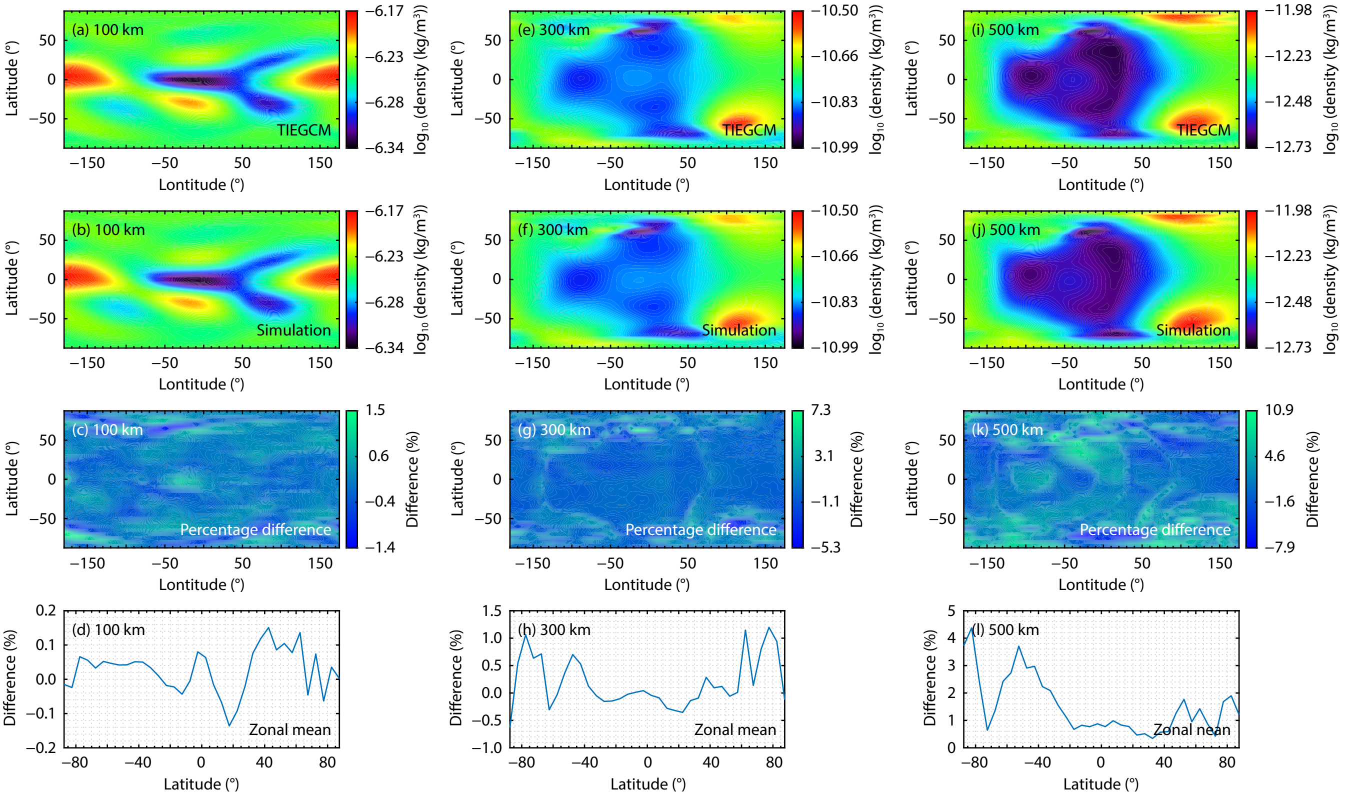

Figure 5. Comparisons between the modeled thermospheric density profiles of the TIEGCM model and the deep learning model at the three considered altitudes of 100 km, 300 km, and 500 km when the $Kp = 7$.

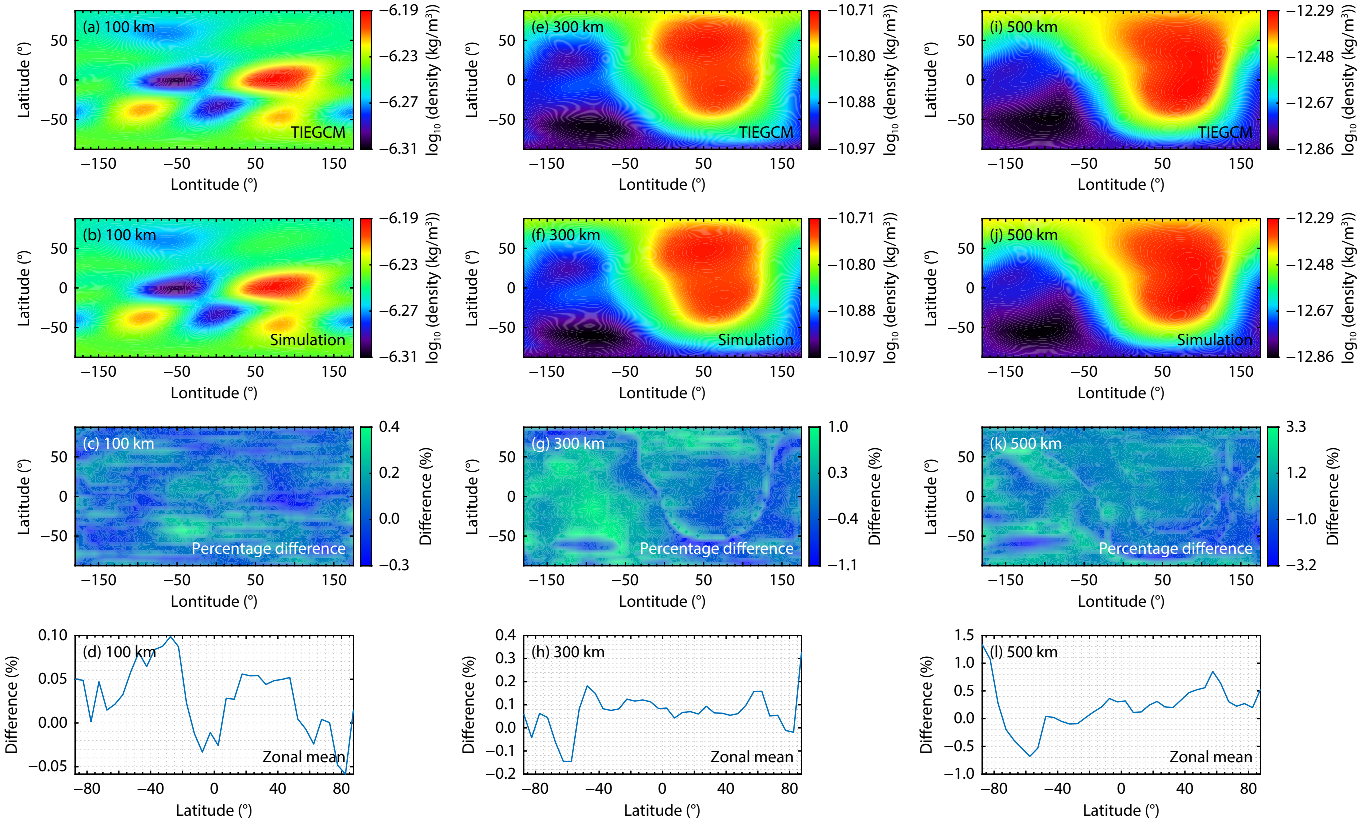

Figure 6. Same as in Figure 5, except for the condition that $Kp = 0$.

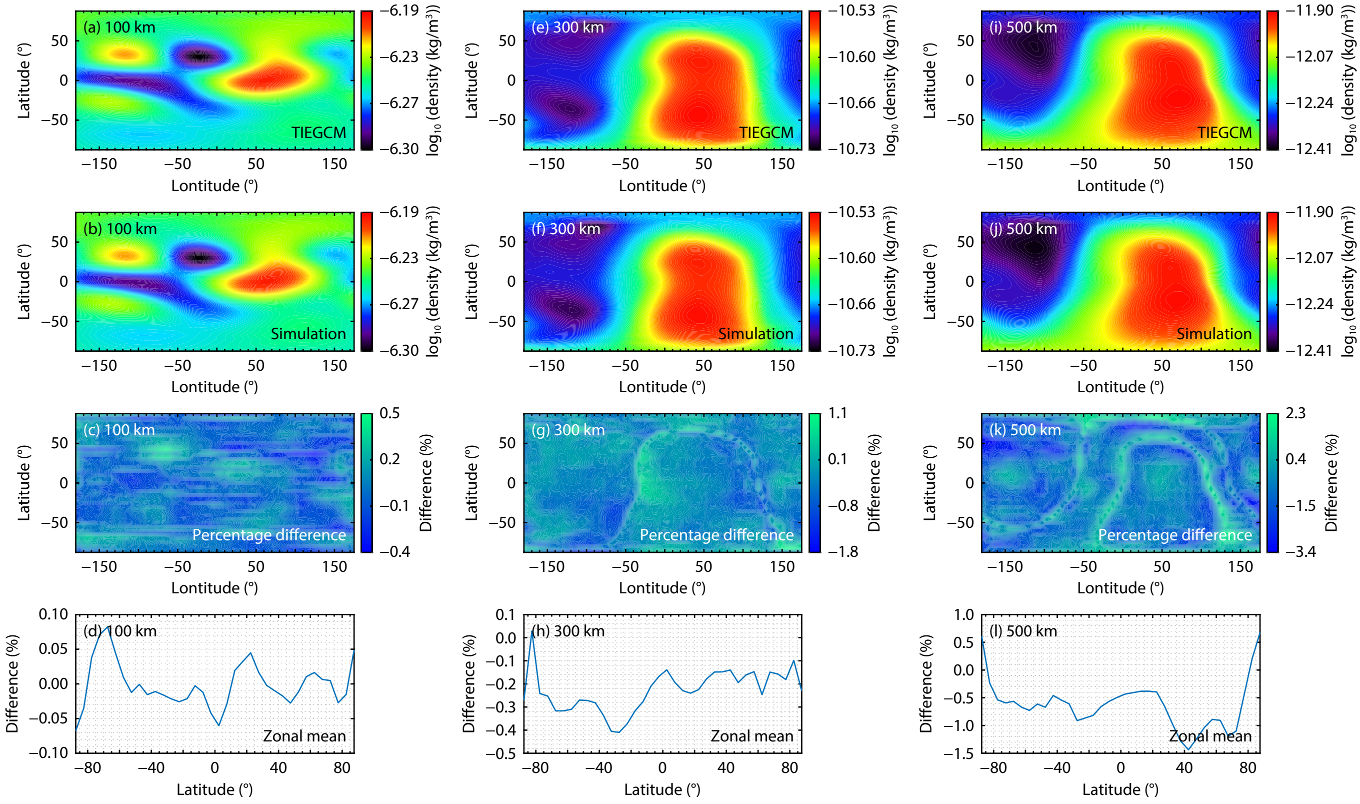

Figure 7. Comparisons between the modeled thermospheric density profiles of the TIEGCM model and the deep learning model at the three considered altitudes of 100 km, 300 km, and 500 km when $F_{10.7} = 174$ sfu.

with *Kp* = 0. At 300 km and 500 km, thermospheric density displays a clear diurnal pattern, characterized by higher values in the afternoon sector (12–24 LT) compared with the morning sector (0–12 LT), a feature accurately captured by the model (Figures 7e, 7f, 7i, 7j). Quantitative comparisons in the lower panels show that the percentage errors are minimal—within −0.05% to 0.1% at 100 km, −0.2% to 0.4% at 300 km, and −1.0% to 1.4% at 500 km. The gradual increase in error with altitude is likely due to the reduced representation of high-altitude conditions in the training dataset. Nonetheless, overall deviations remain below 1.5%, underscoring the model's robustness and precision under quiet-time scenarios.

In addition to geomagnetic conditions, the model was also assessed under varying levels of solar activity, as shown in Figures 7 and 8. Figure 7 presents a comparison between the TIEGCM and model outputs under enhanced solar input ($F_{10.7}$ = 174 sfu [solar flux units]), whereas Figure 8 shows the results under reduced solar input ($F_{10.7}$ = 93 sfu). In both cases, thermospheric density at 300 km displays a pattern similar to that at 500 km, with higher values in the afternoon sector (12–24 LT) than in the morning sector (0–12 LT), as illustrated in Figures 7e, 7f, 7i, 7j and 8e, 8f, 8i, 8j. Under high solar flux conditions, the thermospheric density exceeds that observed during storm periods (Figure 5) by approximately 28%–42%, highlighting the stronger influence of solar radiative forcing. These variations are captured well by the model, with overall percentage differences relative to TIEGCM remaining below 2%. This result indicates that, despite the enhanced sensitivity of the thermospheric density to solar input, the model maintains high accuracy across both high and low solar activity scenarios.

5. Conclusions and Discussions

In this study, a deep learning model based on a modified U-Net architecture was developed to estimate the global thermospheric mass density. The input parameters include time, geographic coordinates (altitude, geodetic latitude, and longitude), geomagnetic indices (*Kp*, B_z), and solar activity data ($F_{10.7}$ daily, $F_{10.7}$ averaged, and solar wind speed). The model outputs thermospheric density across altitudes ranging from 100 to 500 km. To enhance accuracy, three key improvements were introduced: (1) a gated recurrent unit-augmented attention mechanism was embedded within U-Net skip connections to dynamically recalibrate feature weights across encoder stages; (2) a height-adaptive normalization method was implemented to minimize the influence of altitude on input features; and (3) a composite loss function combining mean absolute error and Laplacian loss was utilized to improve learning stability and estimation precision.

The model was systematically evaluated under various geomagnetic and solar activity conditions. The results show that the percentage difference between the model and TIEGCM outputs remained below 5% in all cases. Specifically, errors ranged from −0.7% to 1.4% under quiet geomagnetic conditions, −0.6% to 4.4% during storm periods, −0.6% to 1.5% under low solar input, and −1.4% to 0.6% under enhanced solar input. The model successfully reproduced key features of thermospheric density variability, including diurnal and seasonal patterns, demonstrating both robustness and reliability for operational estimation.

The main goal of this study was to develop a numerical model with the accuracy of physics-driven models (TIEGCM) and the computation efficiency of empirical models. We therefore

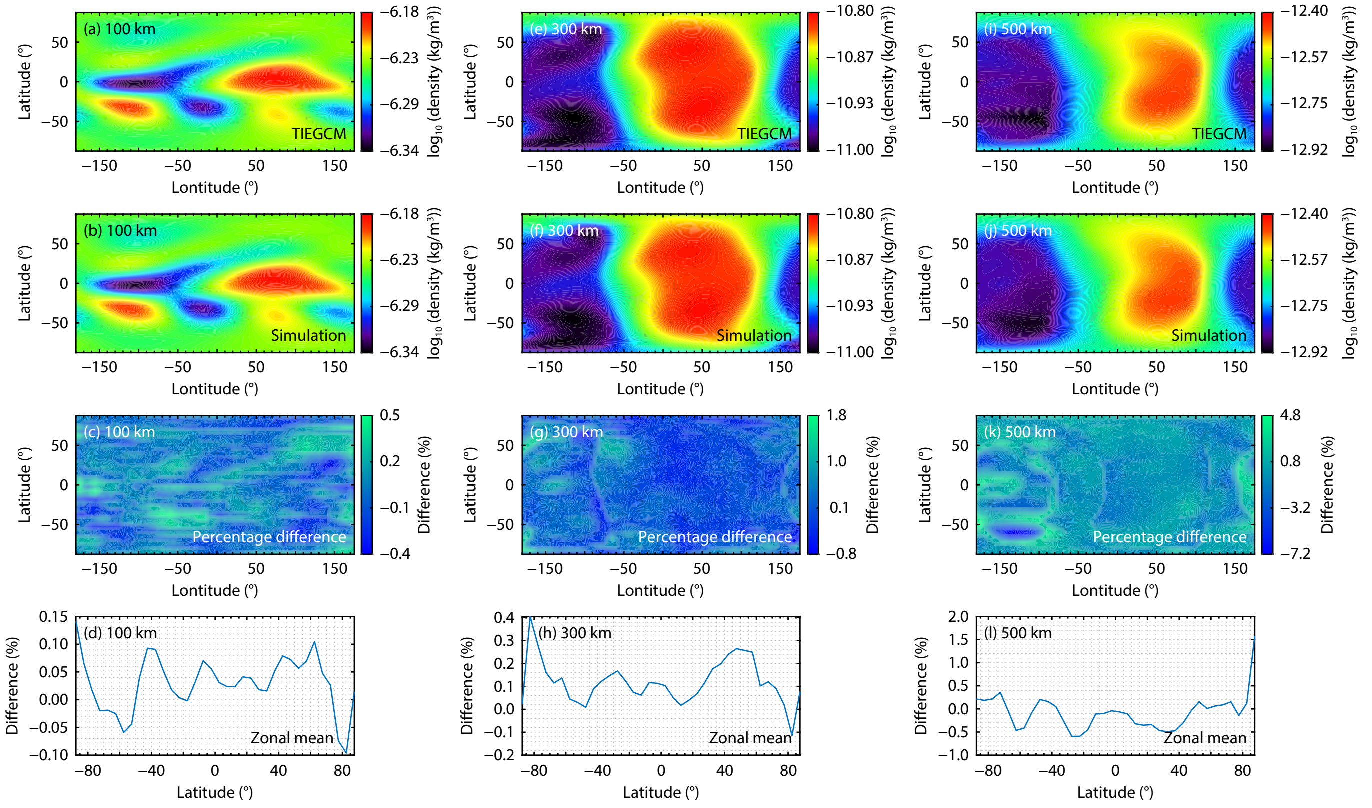

Figure 8. Similar to Figure 7, except for the condition that $F_{10.7}$ = 93 sfu.

prepared the training dataset from TIEGCM simulations, which is a thermosphere–ionosphere general circulation model that solves the three-dimensional momentum, energy, and continuity equations. This model provides a global-wide thermospheric response under intense space weather events that cannot be retrieved from satellite or ground-based measurements. The proposed U-Net model thus learns a nonlinear mapping from input solar or geomagnetic drivers to the thermospheric density and inherits the strengths of the TIEGCM. From a computational standpoint, once trained, the U-Net model can serve as a surrogate for the TIEGCM model to rapidly reconstruct maps of thermospheric density with largely shortened computation time. With the use of one CPU, the computation time for one set of solar and geomagnetic parameters is 14.5 seconds when using the U-Net model but 7.5 minutes when using the TIEGCM model.

Despite these advances, certain limitations remain. Model performance during geomagnetic storms could be further improved by incorporating more storm-time data, as such conditions currently represent less than 15% of the training dataset. The scarcity of storm-related samples limits the model's ability to fully capture storm-specific dynamics. Future efforts should focus on expanding the training set with additional storm-time data to enhance simulative accuracy during disturbed periods. Moreover, although TIEGCM data were exclusively used in this study for their completeness and consistency, integrating real-world measurements could further improve model robustness. Last, incorporating more physically meaningful parameters may help the model better infer underlying physical processes, thereby improving generalization, especially under complex space weather scenarios.

Acknowledgments

This work was supported by the National Natural Science Foundation of China (Grant Nos. 42188101, 42274205, 42025404, 41874195, 42461160256, U2541289, and U25D9004), the National Key R&D Program of China (Grant No. 2022YFF0503700) and the Hubei Province Regional Science and Technology Innovation Plan Project (2025EHA044). The OMNI data can be downloaded from the Goddard Space Flight Center (Papitashvili and King, 2020). A detailed description of the TIEGCM model can be found and downloaded from http://www.hao.ucar.edu/modeling/tgcm/download.php.

References

Azad, R., Aghdam, E. K., Rauland, A., Jia, Y. W., Avval, A. H., Bozorgpour, A., Karimijafarbigloo, S., Cohen, J. P., Adeli, E., and Merhof, D. (2024). Medical image segmentation review: The success of U-Net. *IEEE Trans. Pattern Anal. Mach. Intell.*, *46*(12), 10076–10095. https://doi.org/10.1109/TPAMI.2024.3435571

Barlier, F., Berger, C., Falin, J. L., Kockarts, G., and Thuillier, G. (1978). A thermospheric model based on satellite drag data. *Ann. Geophys.*, *34*, 9–24. https://doi.org/10.1016/b978-0-08-022021-5.50046-x

Bowman, B., Tobiska, W. K., Marcos, F., Huang, C., Lin, C., and Burke, W. (2008). A new empirical thermospheric density model JB2008 using new solar and geomagnetic indices. In *Proceedings of the AIAA/AAS Astrodynamics Specialist Conference and Exhibit*. Honolulu, USA: AIAA. https://doi.org/10.2514/6.2008-6438

Bruinsma, S. (2015). The DTM-2013 thermosphere model. *J. Space Wea. Space Climate*, *5*, A1. https://doi.org/10.1051/swsc/2015001

Bruinsma, S., and Boniface, C. (2021). The operational and research DTM-2020 thermosphere models. *J. Space Wea. Space Climate*, *11*, 47. https://doi.org/10.1051/swsc/2021032

Bruinsma, S. L., Doornbos, E., and Bowman, B. R. (2014). Validation of GOCE densities and evaluation of thermosphere models. *Adv. Space Res.*, *54*(4), 576–585. https://doi.org/10.1016/j.asr.2014.04.008

Chen, Z., Jin, M. W., Deng, Y., Wang, J. S., Huang, H., Deng, X. H., and Huang, C. M. (2019). Improvement of a deep learning algorithm for total electron content maps: Image completion. *J. Geophys. Res. Space Phys.*, *124*(1), 790–800. https://doi.org/10.1029/2018JA026167

Emmert, J. T. (2015). Thermospheric mass density: A review. *Adv. Space Res.*, *56*(5), 773–824. https://doi.org/10.1016/j.asr.2015.05.038

Emmert, J. T., Jones, M. Jr., Siskind, D. E., Drob, D. P., Picone, J. M., Stevens, M. H., Bailey, S. M., Bender, S., Bernath, P. F., … Pérot, K. (2022). NRLMSIS 2.1: An empirical model of nitric oxide incorporated into MSIS. *J. Geophys. Res.: Space Phys.*, *127*(10), e2022JA030896. https://doi.org/10.1029/2022JA030896

Goodfellow, I., Pouget-Abadie, J., Mirza, M., Xu, B., Warde-Farley, D., Ozair, S., Courville, A., and Bengio, Y. (2020). Generative adversarial networks. *Commun. ACM*, *63*(11), 139–144. https://doi.org/10.1145/3422622

Hedin, A. E., Salah, J. E., Evans, J. V., Reber, C. A., Newton, G. P., Spencer, N. W., Kayser, D. C., Alcaydé, D., Bauer, P., … McClure, J. P. (1977). A global thermospheric model based on mass spectrometer and incoherent scatter data MSIS, 1. N_2 density and temperature. *J. Geophys. Res.*, *82*(16), 2139–2147. https://doi.org/10.1029/JA082i016p02139

Hedin, A. E. (1979). Neutral thermospheric composition and thermal structure. *Rev. Geophys.*, *17*(4), 477–485. https://doi.org/10.1029/RG017i004p00477

Hedin, A. E. (1983). A revised thermospheric model based on mass spectrometer and incoherent scatter data: MSIS-83. *J. Geophys. Res.: Space Phys.*, *88*(A12), 10170–10188. https://doi.org/10.1029/JA088iA12p10170

Hedin, A. E. (1987). MSIS-86 thermospheric model. *J. Geophys. Res.: Space Phys.*, *92*(A5), 4649–4662. https://doi.org/10.1029/JA092iA05p04649

Heelis, R. A., Lowell, J. K., and Spiro, R. W. (1982). A model of the high-latitude ionospheric convection pattern. *J. Geophys. Res.: Space Phys.*, *87*(A8), 6339–6345. https://doi.org/10.1029/JA087iA08p06339

Hinton, G., Deng, L., Yu, D., Dahl, G., Mohamed, A. R., Jaitly, N., Senior, A., Vanhoucke, V., Nguyen, P., … Kingsbury, B. (2012). Deep neural networks for acoustic modeling in speech recognition: The shared views of four research groups. *IEEE Signal Process. Mag.*, *29*(6), 82–97. https://doi.org/10.1109/MSP.2012.2205597

Hou, Q. Q., and Liu, F. (2019). Context-aware image matting for simultaneous foreground and alpha estimation. In *Proceedings of the* IEEE/CVF International Conference on Computer Vision (pp. 4129-4138). Seoul, Korea (South): IEEE. https://doi.org/10.1109/ICCV.2019.00423

Ioffe, S., and Szegedy, C. (2015). Batch normalization: Accelerating deep network training by reducing internal covariate shift. In *Proceedings of the 32nd International Conference on Machine Learning* (pp. 448–456). Lille, France: JMLR.

Jacchia, L. G. (1959). Corpuscular radiation and the acceleration of artificial satellites. *Nature*, *183*(4676), 1662–1663. https://doi.org/10.1038/1831662a0

Jacchia, L. G. (1965). *Static Diffusion Models of the Upper Atmosphere with Empirical Temperature Profiles*. Washington: Smithsonian Institution. https://doi.org/10.5962/bhl.title.4246

Jacchia, L. G. (1970). *New static models of the thermosphere and exosphere with empirical temperature profiles*. SAO Special Report No. 313. Cambridge, MA, USA: Smithsonian Astrophysical Observatory. Available at: https://ntrs.nasa.gov/citations/19700027590.

Kingma, D. P., and Ba, L. J. (2015). Adam: A method for stochastic optimization. In *Proceedings of the 3rd International Conference on Learning Representations*. San Diego, USA: ICLR.

Krizhevsky, A., Sutskever, I., and Hinton, G. E. (2017). ImageNet classification with deep convolutional neural networks. *Commun. ACM*, *60*(6), 84–90. https://doi.org/10.1145/3065386

Lecun, Y., Bottou, L., Bengio, Y., and Haffner, P. (1998). Gradient-based learning applied to document recognition. *Proc. IEEE*, *86*(11), 2278–2324. https://doi.org/10.1109/5.726791

LeCun, Y., Bengio, Y., and Hinton, G. (2015). Deep learning. *Nature*, *521*(7553), 436–444. https://doi.org/10.1038/nature14539

Lei, J. H., Li, R. X., Ren, D. X., Weng, L. B., and Ruan, H. B. (2023). Recent progress on the retrieval and modeling of thermosphere mass density. *Rev. Geophys. Planet. Phys. (in Chinese)*, *54*(4), 434–454. https://doi.org/10.19975/j.dqyxx.2022-047

Li, R. X., and Lei, J. H. (2021). Responses of thermospheric mass densities to the October 2016 and September 2017 geomagnetic storms revealed from multiple satellite observations. *J. Geophys. Res.: Space Phys.*, *126*(1), e2020JA028534. https://doi.org/10.1029/2020JA028534

Li Y. P., Sun Y. Q., Zhang X. G., Ai J. Z., Zheng X. L., Li J., Wang Y. J., Guo B. B., Yan F., Wei S. L., Tang X. C., and Cao Y. Y. (2024). Thermosphere joint observations by TM-1 constellations and Swarm-B during the April 2023 geomagnetic storm. *Earth Planet. Phys.*, *8*(2), 307–316. https://doi.org/10.26464/epp2024002

Li, Z., Knipp, D., Wang, W. B., Shi, Y. N., Wang, M., Su, Y., and Li, J. Y. (2019). An EOFs study of thermospheric nitric oxide flux based on TIEGCM simulations. *J. Geophys. Res.: Space Phys.*, *124*(11), 9695–9708. https://doi.org/10.1029/2019JA027004

Licata, R. J., Mehta, P. M., Weimer, D. R., Tobiska, W. K., and Yoshii, J. (2022). MSIS-UQ: Calibrated and enhanced NRLMSIS 2.0 model with uncertainty quantification. *Space Wea.*, *20*(11), e2022SW003267. https://doi.org/10.1029/2022SW003267

Lipton, Z. C., Berkowitz, J., and Elkan, C. (2015). A critical review of recurrent neural networks for sequence learning. arXiv: 1506.00019. https://doi.org/10.48550/arXiv.1506.00019.

Liu, H. L., Foster, B. T., Hagan, M. E., McInerney, J. M., Maute, A., Qian, L., Richmond, A. D., Roble, R. G., Solomon, S. C., … Oberheide, J. (2010). Thermosphere extension of the whole atmosphere community climate model. *J. Geophys. Res.: Space Phys.*, *115*(A12), 2010JA015586. https://doi.org/10.1029/2010JA015586

Liu, X., Thayer, J. P., Burns, A., Wang, W., and Sutton, E. (2014). Altitude variations in the thermosphere mass density response to geomagnetic activity during the recent solar minimum. *J. Geophys. Res.: Space Phys.*, *119*(3), 2160–2177. https://doi.org/10.1002/2013JA019453

McLaughlin, C. A., Hiatt, A., and Lechtenberg, T. (2011). Precision orbit derived total density. *J. Spacecr. Rockets*, *48*(1), 166–174. https://doi.org/10.2514/1.47624

Mehta, P. M., Walker, A., Lawrence, E., Linares, R., Higdon, D., and Koller, J. (2014). Modeling satellite drag coefficients with response surfaces. *Adv. Space Res.*, *54*(8), 1590–1607. https://doi.org/10.1016/j.asr.2014.06.033

Pan, Q., Xiong, C., Lühr, H., Smirnov, A., Huang, Y. Y., Xu, C. Y., Yang, X., Zhou, Y. L., and Hu, Y. (2024). Machine learning based modeling of thermospheric mass density. *Space Wea.*, *22*(5), e2023SW003844. https://doi.org/10.1029/2023SW003844

Papitashvili, N. E., and King, J. H. (2020). OMNI hourly data set [Data set]. *Space Physics Data Facility*. https://doi.org/10.48322/1shr-ht18

Picone, J. M., Hedin, A. E., Drob, D. P., and Aikin, A. C. (2002). NRLMSISE-00 empirical model of the atmosphere: Statistical comparisons and scientific issues. *J. Geophys. Res.: Space Phys.*, *107*(A12), 1468. https://doi.org/10.1029/2002JA009430

Powell, J. (2018). Atmospheric factors and features. In J. Powell (Ed.), *Rare Astronomical Sights and Sounds* (pp. 105–130). Cham: Springer. https://doi.org/10.1007/978-3-319-97701-0_8

Prechelt, L. (2012). Early stopping — But when? In G. Montavon, et al. (Eds.), *Neural Networks: Tricks of the Trade* (2nd ed, pp. 53–67). Berlin: Springer. https://doi.org/10.1007/978-3-642-35289-8_5

Prölss, G. W. (1997). Magnetic storm associated perturbations of the upper atmosphere. In B. T. Tsurutani, et al. (Eds.), *Magnetic Storms* (pp. 227–241). Washington: American Geophysical Union. https://doi.org/10.1029/GM098p0227

Prölss, G. W. (2011). Density perturbations in the upper atmosphere caused by the dissipation of solar wind energy. *Surv. Geophys.*, *32*(2), 101–195. https://doi.org/10.1007/s10712-010-9104-0

Qian, L. Y., Burns, A. G., Emery, B. A., Foster, B., Lu, G., Maute, A., Richmond, A. D., Roble, R. G., Solomon, S. C., and Wang, W. B. (2014). The NCAR TIE-GCM: A community model of the coupled thermosphere/ionosphere system. In J. Huba, et al. (Eds.), *Modeling the Ionosphere–Thermosphere System* (pp. 73–83). Washington: American Geophysical Union. https://doi.org/10.1002/9781118704417.ch7

Ren, D. X., and Lei, J. H. (2022). A long-range forecasting model for the thermosphere based on the intelligent optimized particle filtering. *Sci. China Earth Sci.*, *65*(1), 75–86. https://doi.org/10.1007/s11430-021-9847-9

Ren, X. C., Zhao, B. Q., Ren, Z. P., Wang, Y., and Xiong, B. (2024). Deep learning-based prediction of global ionospheric TEC during storm periods: Mixed CNN-BiLSTM method. *Space Wea.*, *22*(7), e2024SW003877. https://doi.org/10.1029/2024SW003877

Richards, P. G., Torr, M. R., and Torr, D. G. (1981). Solar EUV energy budget of the thermosphere. *Adv. Space Res.*, *1*(12), 53–61. https://doi.org/10.1016/0273-1177(81)90417-8

Ridley, A. J., Deng, Y., and Tóth, G. (2006). The global ionosphere–thermosphere model. *J. Atmos. Sol. Terr. Phys.*, *68*(8), 839–864. https://doi.org/10.1016/j.jastp.2006.01.008

Ronneberger, O., Fischer, P., and Brox, T. (2015). U-Net: Convolutional networks for biomedical image segmentation. In *Proceedings of the 18th International Conference on Medical Image Computing and Computer-Assisted Intervention* (pp. 234–241). Munich, Germany: Springer. https://doi.org/10.1007/978-3-319-24574-4_28

Ruan, H. B., Lei, J. H., Dou, X. K., Liu, S. Q., and Aa, E. (2018). An exospheric temperature model based on CHAMP observations and TIEGCM simulations. *Space Wea.*, *16*(2), 147–156. https://doi.org/10.1002/2017SW001759

Santoso A., Sismanto S., Priyatikanto R., Hartantyo E., and Martiningrum D. R. (2025). The intensity of geomagnetic storms associated with the interplanetary magnetic field and solar wind parameters during Solar Cycle 24. *Earth Planet. Phys.*, *9*(2), 375–386. https://doi.org/10.26464/epp2024069

Shi, H. Q., Xu, W., Ni, B. B., Gu, X. D., Wang, S. W., Feng, J. Y., Cheng, W., Ma, W. C., Xu, H. T., … Zhai, D. F. (2025). Predicting the spatial distribution of VLF transmitter signals using transfer learning models. *Remote Sens.*, *17*(5), 871. https://doi.org/10.3390/rs17050871

Sutskever, I., Vinyals, O., and Le, Q. V. (2014). Sequence to sequence learning with neural networks. In *Proceedings of the 28th International Conference on Neural Information Processing Systems* (pp. 3104–3112). Montreal, Canada: MIT Press.

Trebeschi, S., van Griethuysen, J. J. M., Lambregts, D. M. J., Lahaye, M. J., Parmar, C., Bakers, F. C. H., Peters, N. H. G. M., Beets-Tan, R. G. H., and Aerts, H. J. W. L. (2017). Deep learning for fully-automated localization and segmentation of rectal cancer on multiparametric MR. *Sci. Rep.*, *7*(1), 5301. https://doi.org/10.1038/s41598-017-05728-9

Walczak, S. (2019). Artificial neural networks. In *Advanced Methodologies and Technologies in Artificial Intelligence, Computer Simulation, and Human-Computer Interaction* (pp. 40–53). IGI Global Scientific Publishing, https://doi.org/10.4018/978-1-5225-7368-5.ch004

Wang, P., Fan, E., and Wang, P. (2021). Comparative analysis of image classification algorithms based on traditional machine learning and deep learning. *Pattern Recognit. Lett.*, *141*, 61–67. https://doi.org/10.1016/j.patrec.2020.07.042

Wang, X., Miao, J., Aa, E., Ren, T. L., Wang, Y. X., Liu, J., and Liu, S. Q. (2020). Statistical analysis of Joule heating and thermosphere response during geomagnetic storms of different magnitudes. *J. Geophys. Res.: Space Phys.*, *125*(8), e2020JA027966. https://doi.org/10.1029/2020JA027966

Weng, L. B., Lei, J. H., Zhong, J. H., Dou, X. K., and Fang, H. X. (2020). A machine-learning approach to derive long-term trends of thermospheric density. *Geophys. Res. Lett.*, *47*(6), e2020GL087140. https://doi.org/10.1029/2020GL087140

Xie, B., Cao, J. L., Xie, J., Khan, F. S., and Pang, Y. W. (2024). SED: A simple encoder-decoder for open-vocabulary semantic segmentation. In *Proceedings of the 2024 IEEECVF Conference on Computer Vision and Pattern Recognition* (pp. 3426–3436). Seattle, USA: IEEE. https://doi.org/10.1109/CVPR52733.2024.00329

Xiong, P., Zhai, D. L., Long, C., Zhou, H. Y., Zhang, X. M., and Shen, X. H. (2021). Long short-term memory neural network for ionospheric total electron content forecasting over China. *Space Wea.*, *19*(4), e2020SW002706. https://doi.org/10.1029/2020SW002706

Yu, B. K., Tian, P. H., Xue, X. H., Scott, C. J., Ye, H. L., Wu, J. F., Yi, W., Chen, T. D., and Dou, X. K. (2025). Comparative analysis of empirical and deep learning models for ionospheric sporadic E layer prediction. *Earth Planet. Phys.*, *9*(1), 10–19. https://doi.org/10.26464/epp2024048